Article

Spectroscopic and Electronic Structure Studies of Phenolate Cu(II) Complexes: Phenolate Ring Orientation and Activation Related to Cofactor Biogenesis

Somdatta Ghosh, Jordi Cirera, Michael A. Vance, Tetsuya Ono, Kiyoshi Fujisawa, and Edward I. Solomon

J. Am. Chem. Soc., **2008**, 130 (48), 16262-16273 • DOI: 10.1021/ja8044986 • Publication Date (Web): 08 November 2008

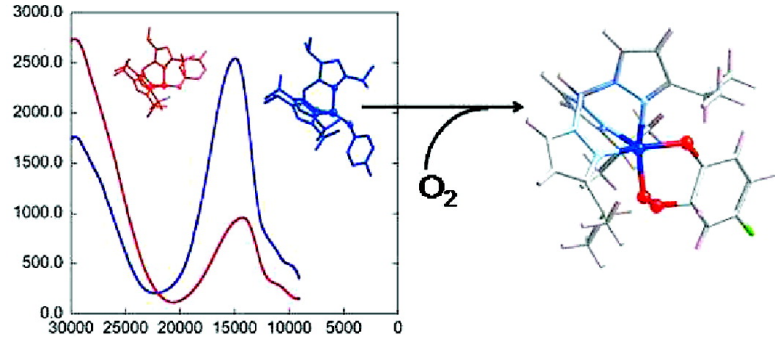

More About This Article

Additional resources and features associated with this article are available within the HTML version:

- Supporting Information
- Access to high resolution figures
- Links to articles and content related to this article
- Copyright permission to reproduce figures and/or text from this article

View the Full Text HTML

J|A|C|S
ARTICLES

Published on Web 11/08/2008

Spectroscopic and Electronic Structure Studies of Phenolate Cu(II) Complexes: Phenolate Ring Orientation and Activation Related to Cofactor Biogenesis

Somdatta Ghosh,[†] Jordi Cirera,[†] Michael A. Vance,[†] Tetsuya Ono,[‡] Kiyoshi Fujisawa,*[,‡] and Edward I. Solomon*[,†]

Department of Chemistry, Stanford University, Stanford, California 94305, and Department of Chemistry, Graduate School of Pure and Applied Sciences, University of Tsukuba, Tsukuba 305-8571, Japan

Received June 12, 2008; E-mail: edward.solomon@stanford.edu

Abstract: A combination of spectroscopies and DFT calculations have been used to define the electronic structures of two crystallographically defined Cu^{II}-phenolate complexes. These complexes differ in the orientation of the phenolate ring which results in different bonding interactions of the phenolate donor orbitals with the Cu^{II}, which are reflected in the very different spectroscopic properties of the two complexes. These differences in electronic structures lead to significant differences in DFT calculated reactivities with oxygen. These calculations suggest that oxygen activation via a Cu^{I} phenoxyl ligand-to-metal charge transfer complex is highly endergonic (>50 kcal/mol), hence an unlikely pathway. Rather, the two-electron oxidation of the phenolate forming a bridging Cu^{II} peroxoquinone complex is more favorable (11.3 kcal/mol). The role of the oxidized metal in mediating this two-electron oxidation of the coordinated phenolate and its relevance to the biogenesis of the covalently bound topa quinone in amine oxidase are discussed.

1. Introduction

Cu sites are ubiquitous in nature and perform a wide variety of functions.[1] There are mononuclear (amine oxidase, galactose oxidase, nitrite reductase), binuclear (hemocyanin, tyrosinase), trinuclear (multicopper oxidases, e.g., laccase), and tetranuclear (nitrous oxide reductase) copper active sites performing electron transfer, oxygen binding, activation and reduction, and nitrogen metabolism.[2,3] Amine oxidase and galactose oxidase are enzymes involved in the two-electron reduction of dioxygen to hydrogen peroxide.[4] These enzymes are particularly interesting because both enzymes undergo a copper-catalyzed biogenesis reaction to create a covalently bound organic cofactor (2,4,5-trihydroxy phenylalanine quinone (TPQ) for amine oxidase[5−10] and a thio-ether linked tyrosyl radical for galactose oxidase) in a post-translational modification of a tyrosine residue.[11,12] The resultant active site then performs the associated oxidase reaction.

The preprocessed form of amine oxidase (anaerobic copper loaded to the apo enzyme) has Cu^{II} bound to three histidine ligands with a tyrosine ~2.6 Å away from the copper center in a distorted trigonal pyramidal geometry (Figure 1A).[13] In the presence of oxygen, the tyrosine residue is proposed to coordinate to Cu^{II} forming a ligand-to-metal charge transfer (LMCT) complex in the first step of the biogenesis of TPQ.[14,15] It is thus important to understand the nature of the Cu^{II}-phenolate bond which leads to the activation of the phenolate ring for oxygen attack. This is a particularly interesting reaction since rather than a reduced copper activating oxygen, this reaction involves an oxidized copper activating the tyrosine substrate. An analogous reaction occurs for intradiol dioxygenases where high-spin Fe^{III} activates the catechol substrate.[16−18] For this reaction it has been shown that a LMCT process can overcome the spin forbidden nature of the reaction of triplet oxygen with the singlet substrate.[19]

[†] Stanford University.
[‡] University of Tsukuba.

(1) Holm, R. H.; Kennepohl, P.; Solomon, E. I. *Chem. Rev.* **1996**, *96*, 2239.
(2) Solomon, E. I.; Chen, P.; Metz, M.; Lee, S.; Palmer, A. E. *Angew. Chem. Intl. Ed.* **2001**, *40*, 4570.
(3) Solomon, E. I.; Sarangi, R.; Woertink, J. S.; Augustine, A. J.; Yoon, J.; Ghosh, S. *Acc. Chem. Res.* **2007**, *40*, 581.
(4) Klinman, J. P. *Chem. Rev.* **1996**, *96*, 2541.
(5) Janes, S. M.; Mu, D.; Wemmer, D.; Smith, A. J.; Kaur, S.; Maltby, D.; Burlingame, A. L.; Klinman, J. P. *Science* **1990**, *248*, 981.
(6) Mu, D.; Medzihradszky, K. F.; Adams, G. W.; Mayer, P.; Hines, W. M.; Burlingame, A. L.; Smith, A. J.; Cai, D.; Klinman, J. P. *J. Biol. Chem.* **1994**, *269*, 9926.
(7) Cai, D.; Klinman, J. P. *J. Biol. Chem.* **1994**, *269*, 32039.
(8) Cooper, R. A.; Knowles, P. F.; Brown, D. E.; McGuirl, M. A.; Dooley, D. M. *Biochem. J.* **1992**, *288*, 337.
(9) Matsuzaki, R.; Fukui, T.; Sato, H.; Ozaki, Y.; Tanizawa, K. *FEBS Lett.* **1994**, *351*, 360.
(10) Nakamura, N.; Matsuzaki, R.; Choi, Y.; Tanizawa, K.; Sanders-Loehr, J. *J. Biol. Chem.* **1996**, *271*, 4718.
(11) McGuirl, M. A.; Dooley, D. M. *Curr. Opin. Chem. Biol.* **1999**, *3*, 138.
(12) Firbank, S. J.; Rogers, M.; Hurtado-Guerrero, R.; Dooley, D. M.; Halcrow, M. A.; Phillips, S. E. V.; Knowles, P. F.; McPherson, M. J. *Biochem. Soc. Trans.* **2003**, *31*, 506.
(13) Kim, M.; Okajima, T.; Kishishita, S.; Yoshimura, M.; Kawamori, A.; Tanizawa, K.; Yamaguchi, H. *Nat. Struct. Biol.* **2002**, *9*, 591.
(14) Dove, J. E.; Schwartz, B.; Williams, N. K.; Klinman, J. P. *Biochem.* **2000**, *39*, 3690.
(15) Schwartz, B.; Dove, J. E.; Klinman, J. P. *Biochem.* **2000**, *39*, 3699.

10.1021/ja8044986 CCC: $40.75

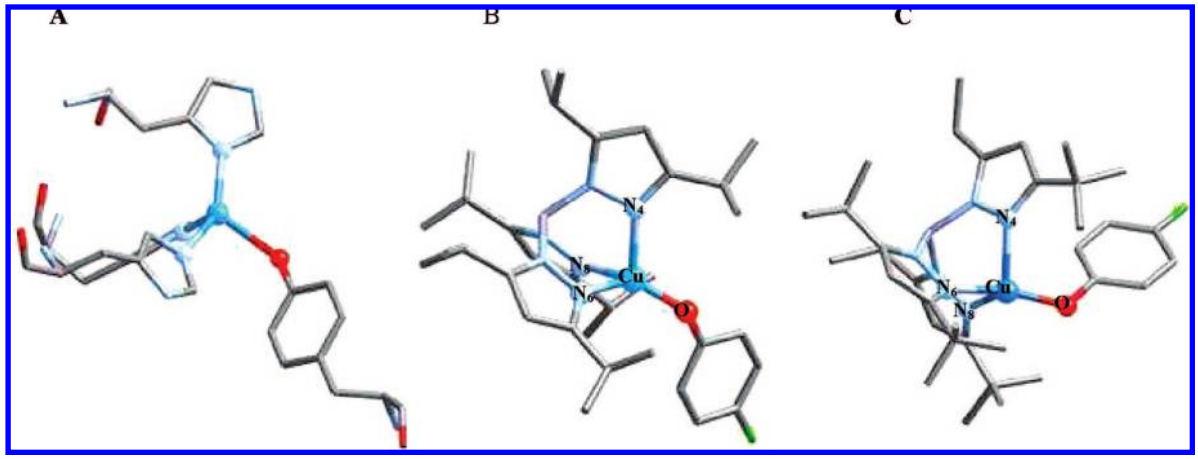

Figure 1. Crystal structures of (A) preprocessed amine oxidase (PDB ID 1IVU) and model complexes (B) [Cu(OPh-4-F){HB(3,5-*i*Pr$_2$pz)$_3$}] and (C) [Cu(OPh-4-F){HB(3-*t*Bu-5-*i*Prpz)$_3$}].

A previously reported Cu-phenolate complex [Cu(OPh-4-F){HB(3,5-*i*Pr$_2$pz)$_3$}][20] (Figure 1B) is an excellent model for the active site of preprocessed amine oxidase and provides the opportunity to investigate the Cu-phenolate bonding and activation which can be used to understand the Cu-tyrosine interaction in amine oxidase. A second Cu^{II}-phenolate complex, [Cu(OPh-4-F){HB(3-*t*Bu-5-*i*Prpz)$_3$}], has been prepared and structurally characterized (reported here, Figure 1C). The key difference between the two model complexes is in the orientation of the phenolate ring because of steric constraints imposed by the hydrotris(pyrazolyl)borate ligand substituents (Figure 1B,C). In this study we use a combination of spectroscopies and density functional theory calculations to elucidate the electronic structure of these two copper-phenolate model complexes and define how the orientation of the phenolate ring affects reactivity. We further evaluate the energetics of the oxygen reaction with the coordinated phenolate and whether radical character associated with the phenolate bonding to Cu^{II} (i.e., Cu^{II}-$^{-}$OPh $\leftrightarrow$ Cu^{I}-$^{\bullet}$OPh) can contribute to this reaction.

2. Experimental Methods

Materials. All reagents were of the highest grade commercially available and were used without further purification. Phenolate complex [Cu(OPh-4-F){HB(3,5-*i*Pr$_2$pz)$_3$}] (L1) was synthesized as previously reported (yield, 64%; Anal. Calcd. for $C_{33}H_{50}N_6BCuFO$: C, 61.92; H, 7.87; N, 13.13%. Found: C, 62.34; H, 8.09; N, 13.04%.).[20] [Cu(OPh-4-F){HB(3-*t*Bu-5-*i*Prpz)$_3$}] (L3) was synthesized by coupling [Cu(OH){HB(3-*t*Bu-5-*i*Prpz)$_3$}][21] and 4-fluorophenol in dry dichloromethane solvent at −50 °C for one hour. The dark blue solid which crystallized from octane/dichloromethane at −50 °C was then dried over vacuum (yield 48%; Anal. Calcd. for $C_{36}H_{56}N_6BCuFO\cdot0.25CH_2Cl_2$: C, 61.89; H, 8.10; N, 11.95%. Found: C, 61.81; H, 8.10; N, 12.24%).

Spectroscopic Studies. Low-temperature absorption spectroscopy was performed on a double-beam spectrophotometer (Cary 500) using a liquid helium cryostat (Janis Research Super Vari-Temp). Low-temperature solution spectra were also collected at −50 °C using a UV−vis diode array spectrophotometer (Agilent 8453, Otsuka Electronics MCPD 2000 with optical fiber attachment). MCD data were collected on CD spectropolarimeters (JASCO J810 with an S20 p.m. tube for the UV/vis region, and a JASCO J200 with an InSb detector for the near-IR region) with sample compartments modified to accommodate magnetocryostats (Oxford Instruments, SM4-7T). Mulls were prepared by grinding the solid material in a mortar embedded in dry ice in a glovebag purged with nitrogen gas. The fine powder was suspended in mineral oil and spread between precooled quartz disks. Solution samples were prepared by dissolving the solid in a glassing solvent (1:1 ether:2-methyl tetrahydofuran, or toluene or dichloromethane or dichloromethane/1,2-dichloroethane). It was more difficult to make glassing solution samples of L1 because it is very sensitive to moisture and readily forms a five-coordinate green complex. EPR spectra were obtained using a Bruker EMX spectrometer, ER 041 XG microwave bridge, and ER 4102ST cavity. All X band data were taken at 77 K in a liquid nitrogen finger dewar. EPR spectra were baseline-corrected and simulated using XSophe (Bruker).

Raman spectra were obtained using a series of lines from Kr^+ (Coherent 190CK) and Ar^+ (Coherent Sabre 25/7) ion lasers with incident power ranging from 10 to 50 mW in an ∼135° backscattering configuration. Dye (Rhodamine 6G, Coherent 599) and Ti-Sapphire (Coherent 890) lasers were used for other spectral regions. Scattered light was dispersed through a triple monochromator (Spex 1877 CP, with 1200, 1800, and 2400 groove/mm gratings) and detected with a back-illuminated CCD camera (Princeton Instruments ST-135). Samples contained in NMR tubes were immersed in a liquid nitrogen finger dewar. Background spectra of pure solid Na_2SO_4 (for solid samples) and pure solvent (for solution samples) were taken under the same conditions. Raman peak intensities were referenced to solvent peaks for excitation profiles. Background spectra of charcoal in the same NMR tubes were used for baseline subtraction. Solution spectra were compared with solid sample spectra for both complexes (by resonance Raman for L1 and MCD for L3) and indicated that the molecular structures defined by the crystallography were maintained in solution.

Crystallography. The diffraction data were measured on a Rigaku/MSC Mercury CCD system with graphite monochromated Mo Kα (λ = 0.71069 Å) radiation in a cold nitrogen stream at −80 °C. Crystal was mounted on the tip of a glass

(16) Lipscomb, J. D.; Orville, A. M. In *Degradation of Environmental Pollutants by Microorganisms and Their Metalloenzymes*; Sigel, H., Sigel, A., Eds.; Marcel Dekker, Inc.: New York, 1992; pp 243−298.
(17) Que, L., Jr.; Ho, R. Y. N. *Chem. Rev.* **1996**, *96*, 2607.
(18) Solomon, E. I.; Brunold, T. C.; Davis, M. I.; Kemsley, J. N.; Lee, S. K.; Lehnert, N.; Neese, F.; Skulan, A. J.; Yang, Y.-S.; Zhou, J. *Chem. Rev.* **2000**, *100*, 235.
(19) Pau, M. Y. M.; Lipscomb, J. D.; Solomon, E. I. *Proc. Natl. Acad. Sci.* **2007**, *104*, 18355.
(20) Fujisawa, K.; Iwata, Y.; Kitajima, N.; Higashimura, H.; Kubota, M.; Miyashita, Y.; Yamada, Y.; Okamoto, K.; Moro-oka, Y. *Chem. Lett.* **1999**, *8*, 739.
(21) Fujisawa, K.; Kobayashi, T.; Fujita, K.; Kitajima, N.; Moro-oka, Y.; Miyashita, Y.; Yamada, Y.; Okamoto, K. *Bull. Chem. Soc. Jpn.* **2000**, *73*, 1797.

fiber using a heavy weight oil. The unit cell parameters of this crystal were obtained using Rigaku Daemon software and refined using CrystalClear on all observed reflections.[22] Data using 0.5° intervals in φ and ω for 40 s/frame for L3 were collected with a maximum resolution of 0.77 Å (744 oscillation images). The highly redundant data sets were reduced using CrystalClear and corrected for Lorentz and polarization effects. An empirical absorption correction was applied.[23,24] Structures were solved by direct methods using the program SIR 92.[25] The position of the metal atoms and their first coordination sphere were located from a direct method *E*-map; other non-hydrogen atoms were found in alternating difference Fourier syntheses (DIRDIF-99)[26] and least-squares refinement cycles. These were refined anisotropically during the final cycles (CrystalStructure).[23,24] Hydrogen atoms were placed in calculated positions. Crystallographic data and structure refinement parameters including the final discrepancies (R and R_w) are listed below. Crystallographic data have been deposited at the CCDC, 12 Union Road, Cambridge CB2 1EZ, U.K., and copies can be obtained on request, free of charge, by quoting the publication citation and the deposition numbers: L1,[20] 740598; L3, 644116. For L3: formula = $C_{36}H_{56}BCuFN_6O$, triclinic, space group $P\bar{1}$ (#2), $a = 10.3150(5)$ Å, $b = 10.6042(7)$ Å, $c = 17.8417(7)$ Å, $\alpha = 79.667(8)°$, $\beta = 81.188(9)°$, $\gamma = 84.864(9)°$, $V = 1893.39(17)$ Å^3, $Z = 2$, $D_{calc} = 1.197$ g cm^{-3}, $\mu = 6.166$ cm^{-1}, reflections collected = 15384, unique reflections = 8522, $R_{int} = 0.019$, no. of observations = 7854 ($I > 3\sigma(I)$), $R = 0.0546$, $R_w = 0.0762$.

Computational Details. All density functional theory calculations (DFT) were performed using the Gaussian 03 program (revision C.02). The optimized geometries have been calculated using the BP86[27−29] functional with 38% Hartree−Fock exchange and the triple-ζ quality basis set proposed by Ahlrichs.[30,31] Polarization functions were included for the Cu center. For both complexes frequency calculations were performed to ensure that the geometries are energy minima. Absorption spectra were calculated using time dependent−density functional theory (TD-DFT)[32] with the hybrid functional B3LYP,[28,33] a triple- ζ basis set, and a polarized continuum model (PCM)[34] with a dielectric constant of 8.93 (the experimental solvent was dichloromethane). The TD-DFT results were analyzed using the program Swizard.[35] The PyMolyze program[36,37] was used to obtain the molecular orbital compositions and overlap populations. The electronic **g** matrix and the hyperfine coupling tensor were calculated with the ORCA code,[38,39] using the hybrid functional B3LYP and a triple-ζ quality basis set. The PCM with a dielectric constant of $\varepsilon = 4$ was employed to simulate a protein environment around the model complexes.

Table 1. Crystal Structure Parameters of L1 and L3 Complexes[a]

parameter	L1	L3
Cu−O	1.731(3)	1.837(2)
Cu−N_4	2.043(4)	2.085(3)
Cu−N_6	1.995(4)	1.931(2)
Cu−N_8	2.023(3)	2.046(2)
Cu−O−C	138.0(4)	126.0(2)
O−Cu−N_4	120.1(2)	103.20(9)
O−Cu−N_6	129.8(2)	161.91(9)
O−Cu−N_8	121.1(1)	103.30(9)
N_4−Cu−N_6	90.9(1)	87.0(1)
N_4−Cu−N_8	92.5(1)	109.48(9)
N_6−Cu−N_8	92.9(1)	86.87(9)

[a] All distances are in angstroms and all angles in degrees.

3. Results

3.1. Crystal Structure. The L1 and L3 phenolate complexes (Figure 1) have four-coordinate distorted tetrahedral environments comprised of a hydrotris(pyrazolyl)borate ligand system and a 4-fluoro-phenoxide ring. The complexes differ in the third position substitution of the pyrazole ring (*iso*-propyl substituent for L1 and *tert*-butyl substituent for L3), which lead to different orientations of the phenoxide ring, resulting in different spectroscopic properties (vide infra). Despite the fact that both L1 and L3 have similar Cu−O−C angles (138° for L1 and 126° for L3) the substituents induce very different orientations of the fluorophenolate. For L1, the phenolate ring is almost perpendicular to the Cu−O−C plane, while for L3 the *tert*-butyl groups force the ring to be in the Cu−O−C plane. The Cu−O bond length for L1 is very short (1.73 Å, Table 1). However this can be due to disorder in the crystal structure as the R value is large (see DFT optimization, Section 3.5). L3 has a normal Cu−O bond length of 1.84 Å and a lower R value. The Cu−N bond lengths of L1 are more uniform (1.99, 2.02, 2.04 Å) compared to those of L3, which has one shorter Cu−N bond relative to two longer Cu−N bonds (1.93, 2.05, 2.08 Å). These complexes, which model the active site of the preprocessed enzyme amine oxidase, provide an opportunity to study the effect of orientation of the phenolate ring on the electronic structure and oxygen reactivity of this class of active site.

3.2. Absorption and MCD. The low-temperature solution absorption spectrum and mull MCD data for the L1 complex are presented in Figure 2. The absorption spectrum is dominated by an intense charge transfer (CT) band at ∼14 700 cm^{-1} and a weaker CT band at higher energy (∼28 000 cm^{-1}). The low-temperature solution absorption spectrum of the L3 complex (Figure 3A) has a weak band at ∼14 600 cm^{-1} and a more intense band at ∼28 000 cm^{-1}. This is the opposite intensity distribution compared to the L1 complex. MCD transitions gain intensity at low temperature and high magnetic field through a mechanism that selectively enhances the d → d transitions, which are often weak in absorption. A low-symmetry Cu^{II} complex is expected to show four d → d transitions into the unoccupied β-LUMO. In addition, the phenolate ligand has an out-of-plane (oop) and an in-plane (ip) occupied π valence orbital, which can potentially donate charge into the unoccupied metal 3d orbital (β-LUMO), resulting in two phenolate → Cu^{II} d CT transitions. The tris(pyrazolyl)borate ligand can also generate multiple CT transitions into the unoccupied metal 3d

(22) CrystalClear Ver. 1.3; Pflugrath, J. W. *Acta Crystallogr.* **1999**, *D55*, 1718.
(23) CrystalStructure 3.70 and 3.81, Crystal Structure Analysis Package; Rigaku and Rigaku/MSC, 2005 and 2006.
(24) Watkin, D. J.; Prout, C. K.; Carruthers, J. R.; Betteridge, P. W. Crystal Issue 10; Chemical Crystallography Laboratory: Oxford, U.K., 1996.
(25) Altomare, A.; Cascarano, G.; Giacovazzo, C.; Guagliardi, A.; Burla, M.; Polidori, G.; Camalli, M. *J. Appl. Crystallogr.* **1994**, *27*, 435.
(26) Beurskens, P. T.; Admiraal, G.; Beurskens, G.; Bosman, W. P.; de Gelder, R.; Israel, R.; Smits, J. M. M. DIRDIF-99 program system; Technical Report of the Crystallography Laboratory; University of Nijmegen: The Netherlands, 1999.
(27) Frisch, M. J.; et al. Gaussian 03, Revision C.02.
(28) Becke, A. D. *Phys. Rev. A* **1988**, *38*, 3098.
(29) Perdew, J. P. *Phys. Rev. B* **1986**, *33*, 8822.
(30) Schaefer, A.; Horn, H.; Ahlrichs, R. *J. Chem. Phys.* **1992**, *97*, 2571.
(31) Schaefer, A.; Huber, C.; Ahlrichs, R. *J. Chem. Phys.* **1994**, *100*, 5829.
(32) Casida, M. E.; Jamorski, C.; Casida, K. C.; Salahub, D. R. *J. Chem. Phys.* **1998**, *108*, 4439.
(33) Becke, A. D. *J. Chem. Phys.* **1993**, *98*, 5648.
(34) Miertus, S.; Scrocco, E.; Tomasi, J. *Chem. Phys.* **1981**, *55*, 117.
(35) Gorelsky, S. I. Swizard program; 2008.
(36) Tenderholt, A. L. PyMolyze, 2.0; Stanford; 2007.
(37) O'Boyle, N. M.; Tenderholt, A. L.; Langner, K. M. *J. Comput. Chem.* **2008**, *29*, 839; PyMolyze.
(38) Neese, F.; Solomon, E. I. *Inorg. Chem.* **1998**, *37*, 6568.
(39) Neese, F. *J. Am. Chem. Soc.* **2006**, *128*, 10213.

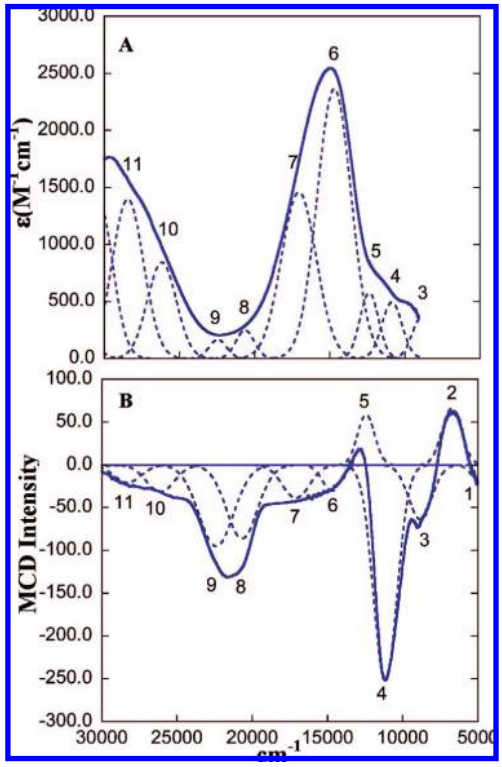

Figure 2. (A) L1 low-temperature solution absorption spectrum in dichloromethane/1,2-dichloroethane; (B) 5 K, 7 T mull MCD spectrum. The Gaussian-resolved bands obtained from a simultaneous fit of the absorption and MCD spectra are shown by dashed lines.

orbital. Simultaneous Gaussian fits of the absorption and MCD spectra resolve these transitions which are presented in Tables 2 and 3.

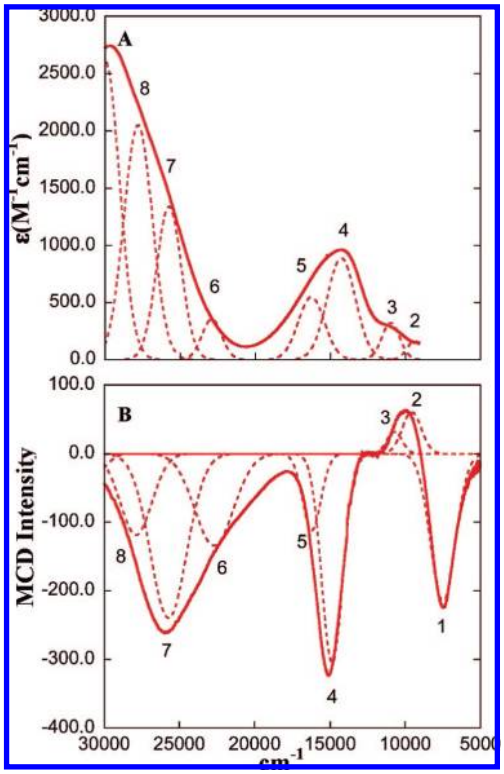

Figure 3. (A) L3 low-temperature solution absorption spectrum in ether/2-methyl THF; (B) 5 K, 7 T mull MCD spectrum. The Gaussian-resolved bands obtained from a simultaneous fit of the absorption and MCD spectra are shown by dashed lines.

Table 2. Gaussian Resolved Peak Positions and Band Assignments from Absorption, MCD, and TD-DFT Spectra of L1

band	energy (cm^{-1})	ε (M^{-1} cm^{-1})	MCD/abs[a]	TD-DFT (cm^{-1})	assignment
1	4849		−	5322	d_{z^2}
2	6745		−	7942	$d_{xz} - d_{yz}$
3	8884	356	−0.179		pyr CT
4	11019	493	−0.514	11632	$d_{xz} + d_{yz}$
5	12409	575	0.102	12176	d*xy*
6	14727	2363	−0.012	16332	oop OPh CT
7	17081	1459	−0.027	20304	pyr CT
8	20669	247	−0.350	23337	pyr CT
9	22432	164	−0.580	24556	pyr CT
10	26147	842	−0.037	24642	ip OPh CT
11	28371	1397	−0.014	26663	pyr CT
12	30322	1377	−0.001	31637	pyr CT

[a] Normalized ratio of MCD intensity to absorption intensity. This ratio approximates the relative *C*/*D* ratios for mull data, where it is not possible to obtain absolute *C*/*D* ratios. Sometimes a CT band might have a high *C*/*D* ratio when there is significant amount of metal character in the transition.

Table 3. Gaussian Resolved Peak Positions and Band Assignments from Absorption, MCD, and TD-DFT Spectra of L3

band	energy (cm^{-1})	ε (M^{-1} cm^{-1})	MCD/abs[a]	TD-DFT (cm^{-1})	assignment
				5100	oop OPh CT
1	7499		−	11225	d_{xz}
2	9483	162	0.376	15078	d_{yz}
3	10860	321	0.100	15574	d_{z^2}
4	14576	890	−0.342	16035	d_{xy}
5	16250	548	−0.205	22083	pyr CT
6	22800	137	−0.379	23836	pyr CT
7	25740	685	−0.178	26598	pyr CT
8	27852	1764	−0.058	28216	ip OPh CT

[a] Normalized ratio of MCD intensity to absorption intensity. This ratio approximates the relative *C*/*D* ratios for mull data, where it is not possible to obtain absolute *C*/*D* ratios. Sometimes a CT band might have a high *C*/*D* ratio when there is significant amount of metal character in the transition.

Generally a higher *C*/*D* ratio (MCD/absorption intensity) for a band indicates a d → d transition. On the basis of the *C*/*D* ratios, the transitions have been categorized as CT (*C*/*D* < 0.01) and d → d bands (*C*/*D* > 0.1) in Tables 2 and 3 for L1 and L3, respectively. Bands 1, 2, 4, and 5 in Figure 2 have been assigned as d → d bands in L1, and bands 1−4 in Figure 3 have been assigned as d → d bands in L3. Since there can be four d → d transitions and there are five bands observed (bands 1−5, Figure 2) in the lower energy region of L1, band 3 can be assigned as a low-energy pyrazole → Cu CT transition. This is based on a previous study of a Cu-thiolate complex of L1.[40] L3 should also show a weak pyrazole $\pi \rightarrow Cu^{II}$ CT transition in this region, but a fifth transition is not required by the data. The ligand field transitions of L3 are blue-shifted compared to L1, indicating a stronger ligand field for L3. In L1, the intense transition at 14 727 cm^{-1} with molar extinction coefficient of 2360 M^{-1} cm^{-1} is assigned as a phenolate → Cu CT transition (see resonance Raman data). Bands 7−12 in L1 are also assigned as CT transitions based on low *C*/*D* values. Importantly, in L3, band 4 at 14 576 cm^{-1} (Figure 3) is very intense in MCD and is assigned as a d → d transition based on its high *C*/*D* ratio (0.34). The higher energy bands in L3 (bands 5−8) are assigned as CT transitions. Detailed assignments of these transitions (presented in Tables 2 and 3) are described in Section 4.2 based on TD-DFT calculations, correlated to the spectra.

(40) Randall, D. W.; G, S., D.; Hedman, B.; Hodgson, K. O.; Fujisawa, K.; Solomon, E. I *J. Am. Chem. Soc.* **2000**, *122*, 11620.

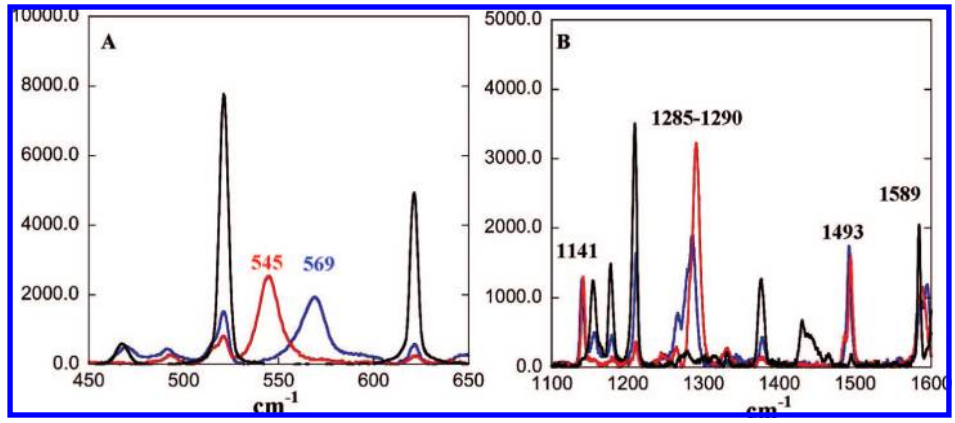

Figure 4. Resonance Raman spectrum of L1 (blue) and L3 (red) in toluene (black): (A) low-frequency Cu−O stretch, (B) high-frequency C−O stretch, excited at 647 nm. Data were collected at 77 K.

3.3. Resonance Raman. The solution resonance Raman spectra of the L1 (blue) and L3 (red) complexes obtained at 77 K with 647 nm excitation are shown in Figure 4. The Cu−O stretch, observed at 569 cm^{-1} in L1, is shifted to 545 cm^{-1} in L3. This indicates that the Cu−O bond is stronger in the L1 complex. Multiple features are observed between 1100−1600 cm^{-1} which are typical of metal phenolate complexes (Figure 4B). The peaks at 1141 cm^{-1} can be assigned as C−H bending modes. The peaks at ∼1285−1290 cm^{-1} are assigned as C−O stretching vibrations. The C−C stretching vibrations appear at ∼1493 and 1598 cm^{-1}.[41,42]

The resonance Raman profile of L1 is shown in Figure 5A. The Cu−O and C−O profiles clearly indicate the presence of two distinct phenolate → Cu CT transitions centered around ∼14 700 cm^{-1} and ∼26 000 cm^{-1}. These two CT transitions can be assigned as the ip and the oop phenolate π CT. For a free phenolate ligand these transitions are separated by 6000 cm^{-1}. Thus this large splitting of the phenolate π orbitals (∼11 000 cm^{-1}) results from coordination to the Cu^{II} (see Section 4.3). The resonance Raman profile of L3 (Figure 5B) shows mainly C−O and some Cu−O enhancement at ∼14 500 cm^{-1}, indicating some phenolate → Cu CT character mixed into this d → d transition (vide infra). There was no Cu−O, C−O, or Cu−N enhancement observed with excitation at higher energies for L3 (Figure 5B).

3.4. EPR. The frozen glass EPR spectra of the complexes with simulations are presented in Figure 6. The EPR parameters are summarized in Table 4. The EPR spectra show that the complexes have an $S = {}^1/_2$ ground state with $g_1 > g_2 > g_3 > 2.0$. The g values are strongly rhombically split which reflects significant d_{z^2} mixing into a $d_{x^2-y^2}$ ground state wave function (see Section 4.1). Also note that the largest hyperfine (A_3) is associated with the smallest g value (g_3), likely reflecting some Cu 4s mixing into the singly occupied d orbital (vide infra).

3.5. Electronic Structure Calculations. For geometry optimizations the L1 and L3 complexes were modeled by replacing the *iso*-propyl and *tert*-butyl groups, respectively, which are not oriented toward the 4-fluorophenolate ring by hydrogen. For both optimized structures frequency calculations and stability checks were performed to ensure the structures converged to energy minima. Table 5 compares the most relevant geometric parameters for L1 and L3 with the crystal structures (see Figure 1 and Table 1 for the labeling of the atoms). Figure 7 gives the overlay of the crystal and optimized structures, showing good agreement between experiment and calculations. The optimized structure of L1 gives a longer Cu−O bond length (1.83 Å) compared to that observed in the crystal structure (1.73 Å). This discrepancy likely reflects the large isotropic thermal pa-

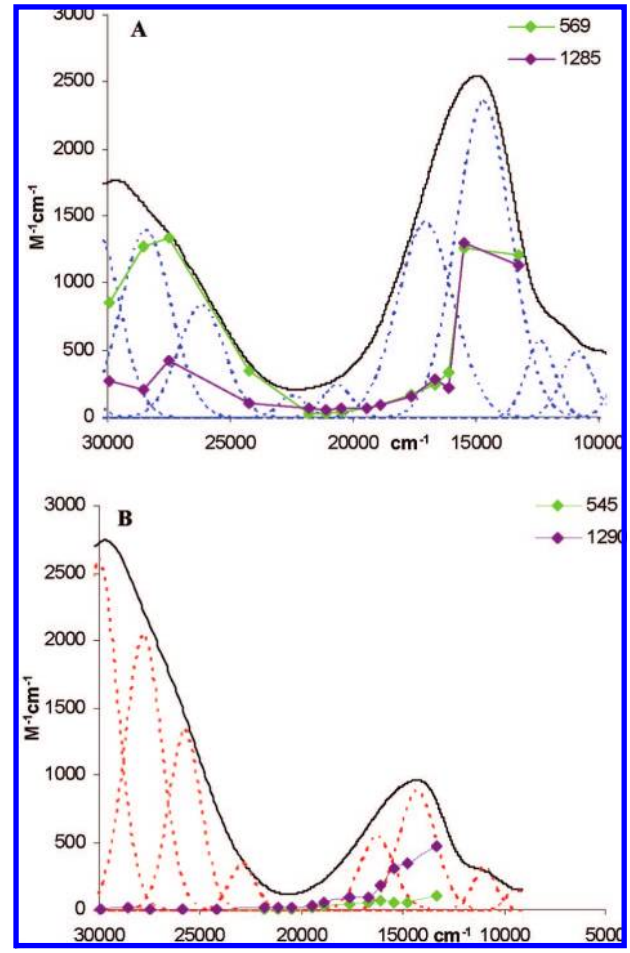

Figure 5. Resonance Raman excitation profiles of Cu−O (green) and C−O (purple) stretches overlaid on the absorption spectrum (solid black line) with Gaussian fits (dotted lines): (A) L1, (B) L3.

(41) Jazdzewski, B. A.; Holland, P. L.; Pink, M.; Young, V. G., Jr.; Spencer, D. J. E.; Tolman, W. B. *Inorg. Chem.* **2001**, *40*, 6097.
(42) Que, L. J. In *Biological Applications of Raman Spectroscopy*; Wiley: New York, 1988; Vol. 3, p 491.

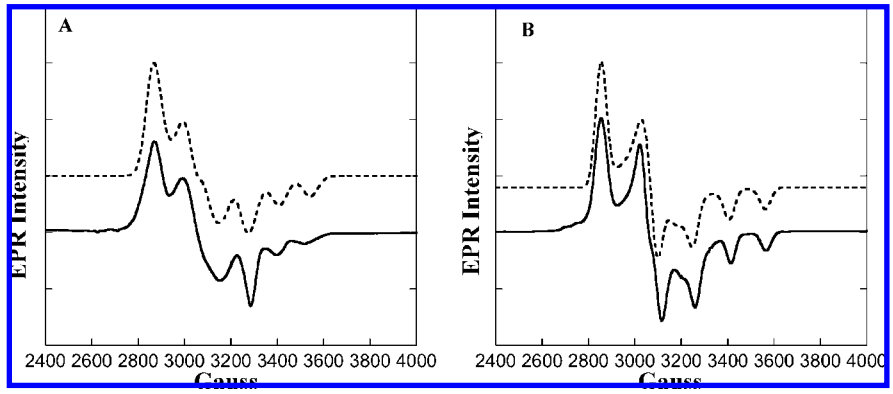

Figure 6. Frozen glass EPR spectra (solid line) and simulation (dotted line) of (A) L1 in dichloromethane/1,2-dichloroethane and (B) L3 in ether/2-methyl THF, at 77K.

Table 4. EPR Parameters of L1 and L3

complex	g_1	g_2	g_3	A_1[a]	A_2[a]	A_3[a]
L1	2.320	2.135	2.01	5	67	120
L3	2.317	2.125	2.005	0	20	143

[a] Values $\times 10^{-4}$ cm^{-1}.

Table 5. Comparison of the Geometric Parameters for L1 and L3 Crystal Structures and Geometry Optimized Structures[a]

L1	crystal	optimized	L3	crystal	optimized
Cu−O	1.732	1.832	Cu−O	1.837	1.823
Cu−N_4	2.043	2.100	Cu−N_4	2.086	2.076
Cu−N_6	1.994	1.952	Cu−N_6	1.931	1.954
Cu−N_8	2.023	2.009	Cu−N_8	2.045	2.085
O−Cu−N_4	120.076	107.238	O−Cu−N_4	103.184	105.753
O−Cu−N_6	129.873	141.642	O−Cu−N_6	161.900	157.761
O−Cu−N_8	121.043	119.425	O−Cu−N_8	103.332	104.279
N_4−Cu−N_6	90.891	90.659	N_4−Cu−N_6	86.972	87.682
N_4−Cu−N_8	92.437	93.549	N_4−Cu−N_8	109.515	105.354
N_6−Cu−N_8	92.980	92.084	N_6−Cu−N_8	86.897	88.609

[a] All distances are in angstroms and all angles in degrees.

rameter in the crystallographic data (B value $\sim$ 9.5).[43] Badger's analysis correlating the resonance Raman stretching frequencies with the bond lengths of L1 and L3 predicts the bond length of L1 to be 1.82 Å, which is close to the theoretically calculated bond length (1.83 Å). The ring orientations in the crystal structures of L1 and L3 are reproduced in the optimized structures.

A comparison of the charge and spin density distribution on the atoms of the optimized L1 and L3 structures is provided in Table 6. These show that the spin density on the phenolate ring is higher and charge is lower for L1 than L3, thus the covalent interaction of the phenolate with Cu^{II} is greater in L1. These computational results indicate that the orientation of the phenolate ring affects its donor interaction with the Cu^{II}.

4. Analysis

4.1. Ground State Wave function. The different orientations of the phenolate ring in L1 and L3 result in very different spectral features. These electronic structure differences experimentally reflect qualitative differences in the molecular orbitals of these complexes. We focus on the five copper d orbitals, the phenolate oop (which is the HOMO for both complexes), and ip (HOMO-4 for L1 and HOMO-10 for L3 in a model without substituents on the hydrotris(pyrazolyl)borate/tpzb ligand) orbitals and the lowest energy tpzb π donor orbital (HOMO-1 in both complexes). Lower energy tpzb orbitals are involved in π and σ donor bonds and contribute to the CT spectra in the higher energy region.

Figure 8 gives these MO diagrams (β orbitals which reflect d $\rightarrow$ d and CT transitions into the β LUMO of Cu) for L1 and L3 with complete MO diagrams provided in the Supporting Information. The MO diagrams show that the occupied d orbitals in L3 are lower in energy (relative to the β LUMO) than L1, indicating a higher ligand field strength in L3 compared to L1, as observed experimentally. The d orbital splitting pattern ($d_{x^2-y^2}$ (β LUMO) > d_{z^2} > d_{xz} − d_{yz} > d_{xz+yz} > d_{xy} for L1 and $d_{x^2-y^2}$ (β LUMO) > d_{xz} > d_{z^2} > d_{yz} > d_{xy} for L3) in the **g** tensor coordinate systems (vide infra) indicate large rhombic distortions.

The different orientations of the phenolate rings of the L1 and L3 complexes result in a major difference in the nature of their β LUMOs (Figure 9). L1 has 56.4% Cu d which is delocalized into the oop phenolate LUMO resulting in a π type ground state (Figure 9A). Alternatively, L3 has 65.1% Cu d which is delocalized into the ip phenolate LUMO which results in a σ bonding interaction with the singly occupied d orbital. This difference in the ground state wave function produces different splittings of the ip and oop phenolate orbitals in the two complexes and results in the large observed spectral differences between these complexes in Figures 2 and 3 (vide infra).

From Figure 9 it is clear that both LUMOs have a contribution of d_{z^2} mixed into the $d_{x^2-y^2}$ orbital. To get this composition of the LUMO, the molecule has been orientated along the principal axes of the electronic **g** tensor. Using this alignment, the d component of the ground state wave function for L1 is $\Psi(L1) = 91.7\%\ d_{x^2-y^2} + 6.9\%\ d_{z^2}$, while for L3 it is $\Psi(L3) = 88.4\%\ d_{x^2-y^2} + 11.5\%\ d_{z^2}$. Thus the mixing of d_{z^2} into $d_{x^2-y^2}$ is larger for L3. This is consistent with the larger rhombicity observed in the EPR spectrum of L3 relative to L1 in Figure 6. The calculated g values in the principal coordinate system, while quantitatively off, reproduce the experimental trend (Table 7). The hyperfine coupling tensor was calculated to be aligned with the **g** matrix giving the A values summarized in Table 7. The calculated A values also are not in quantitative agreement but reproduce the experimental trends. The considerable amount of calculated 4s mixing (1.9% for L1 and 4.9% for L3) results in the highest A value being associated with the lowest g value.

(43) Cramer, C. J.; Tolman, W. B.; Theopold, K. H.; Rheingold, A. L. *Proc. Natl. Acad. Sci.* **2003**, *100*, 3635.

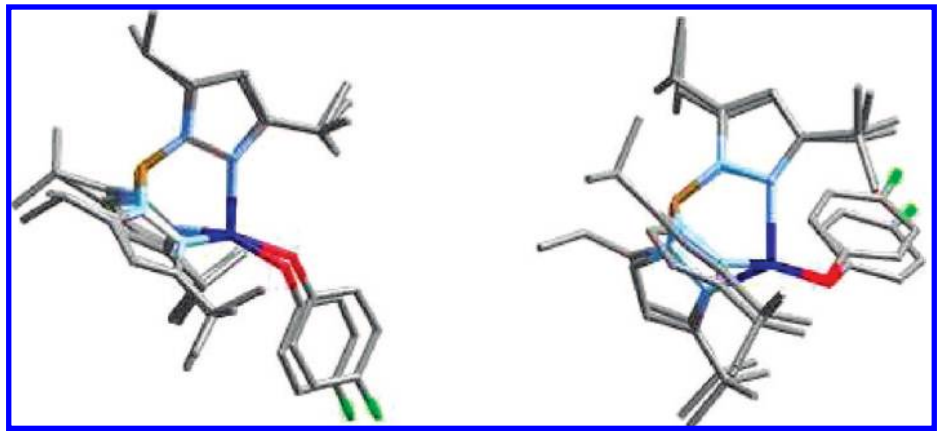

Figure 7. Overlap between the crystal structure and the optimized geometry for L1 (left) and L3 (right).

Table 6. Total Spin Density and Mulliken Charge on the Cu Atom, the OPhF Ligand, and the tpzb for L1 and L3

compd	Cu	phenO	tpzb
L1(spin)	0.742	0.144	0.114
L3(spin)	0.794	0.090	0.117
L1(charge)	1.213	−0.557	−0.655
L3(charge)	1.438	−0.661	−0.777

4.2. Time Dependent DFT Calculations and Spectroscopic Assignments. The absorption spectrum of L1 is dominated by an intense CT band at ~15 000 cm^{-1} and a weaker transition at ~28 000 cm^{-1}. L3 shows bands at similar energies but with an inverse intensity distribution, i.e., the band at ~28 000 cm^{-1} is more intense than the band at ~15 000 cm^{-1} (experimental data from Figures 2A and 3A combined in Figure 10A). TD-DFT calculations on these complexes qualitatively reproduce these experimental energies and intensity distributions (Figure 10B).

The observed electronic transitions of the two complexes (Figures 2, 3) are assigned by combining the experimental and TD-DFT results and are presented in Tables 2 and 3. In L1, bands 2 and 4 (Figure 2, assigned as ligand-field transitions in section 3.2) show a pseudo-*A* term in the MCD spectrum (i.e., derivative shaped, oppositely signed *C* term transitions) characteristic of the d_{xz} and d_{yz} transitions which have effective spin−orbit coupling. TD-DFT calculations assign bands 1, 2, 4, and 5 as the d_{z^2}, $d_{xz} - d_{yz}$, $d_{xz} + d_{yz}$ and $d_{xy} \rightarrow d_{x^2-y^2}$ transitions, respectively. Band 3 is assigned as a low-energy pyrazole $\pi \rightarrow$ Cu $d_{x^2-y^2}$ CT transition. The presence of high-energy pyrazole orbitals in the MO diagram (Figures 8, S1) supports the possibility of a low-energy pyrazole CT band; however, the TD-DFT calculations predict pyrazole CT bands at higher energies (Table 2). Band 6 and 10 (Figure 2) are assigned as phenolate → Cu CT transitions based on the resonance Raman profiles (Figure 5A). TD-DFT calculations are consistent with these assignments and further identify band 6 as the oop phenolate → Cu CT transition and band 10 as the ip phenolate →Cu CT transition. Bands 7−9 and 11, 12 are assigned as pyrazole → Cu CT bands based on the TD-DFT results. Bands 8 and 9 are relatively intense in MCD because they have more metal 3d character (5−9%) covalently mixed into their associated pyrazole donor orbitals.

In the case of L3 (Figure 3), bands 1 and 2 show the pseudo-*A* term, and hence are assigned as the d_{xz} and $d_{yz} \rightarrow d_{x^2-y^2}$ ligand field transitions. On the basis of the signs of the MCD spectrum, bands 3 and 4 are assigned as d_{xy} and $d_{z^2} \rightarrow d_{x^2-y^2}$ transitions, respectively. TD-DFT calculations support these assignments. Importantly, from its C/D value band 4 is assigned as a d → d transition (Section 3.2) even though it has a higher extinction coefficient than most d → d bands (~900 M^{-1} cm^{-1}), and shows some resonance enhancement of the Cu−O vibration (Figure 5B). This high absorption intensity likely reflects the 10% ip phenolate CT character calculated to be mixed into this d→d band. TD-DFT calculations assign band 8 as the ip phenolate → Cu CT transition. These also predict an oop phenolate → Cu CT transition at ~5100 cm^{-1} which is not detected experimentally. Bands 5−7 are assigned as pyrazole CT transitions based on the TD-DFT calculations. Band 7 is calculated to have ~5% metal 3d character mixed into the pyrazole CT transition, resulting in significant MCD intensity. The presence of similar high-energy pyrazole orbitals in the MO diagram (Figure 8 right, S1) predicts a similar low-energy pyrazole $\pi \rightarrow$ Cu CT transition in L3 as in L1; however, such a transition is not resolved in L3 reasonably due to overlapping transitions.

4.3. Phenolate-Cu(II) Bonding. As indicated above the phenolate ligand has two valence orbitals available for bonding to Cu^{II}; these are the oxygen *p*-orbitals ip and oop of the aromatic ring and delocalized into the ring (Scheme 1). In the free phenolate ligand these orbitals are split by ~6000 cm^{-1}, the ip orbital (O coefficient = 79.6%) being more stable than the oop orbital (O coefficient = 36.8%). When the oxygen of the phenolate ligand is bound to a charged metal ion with little covalency (e.g., Zn^{II}, Scheme 1), this splitting increases to ~20 000 cm^{-1} (in both L1 and L3 orientations). When the phenolate ligand is bound to the Cu^{II} tpzb ligand in the L1 and L3 orientations, the splitting between the ip and oop orbitals is calculated to be ~16 600 cm^{-1} and 23 200 cm^{-1}, respectively. The different splitting in the L1 and L3 complexes is associated with the different bonding interactions of these orbitals with the singly occupied MO of Cu^{II} in the two complexes due to the different orientation of the phenolate plane relative to the Cu−O bond (see β LUMOs in Figure 9).

In the case of L1, the higher energy oop phenolate orbital has a strong bonding interaction with the LUMO (Figure 9A), thus it is stabilized. This results in a decrease in the energy difference between the nonbonding ip orbital and the bonding oop orbital relative to the splitting in the Zn^{II} reference complex. The good overlap between the oop phenolate orbital and the β LUMO results in an intense low-energy CT transition as observed (band 6, Figure 2). This is far more intense than the

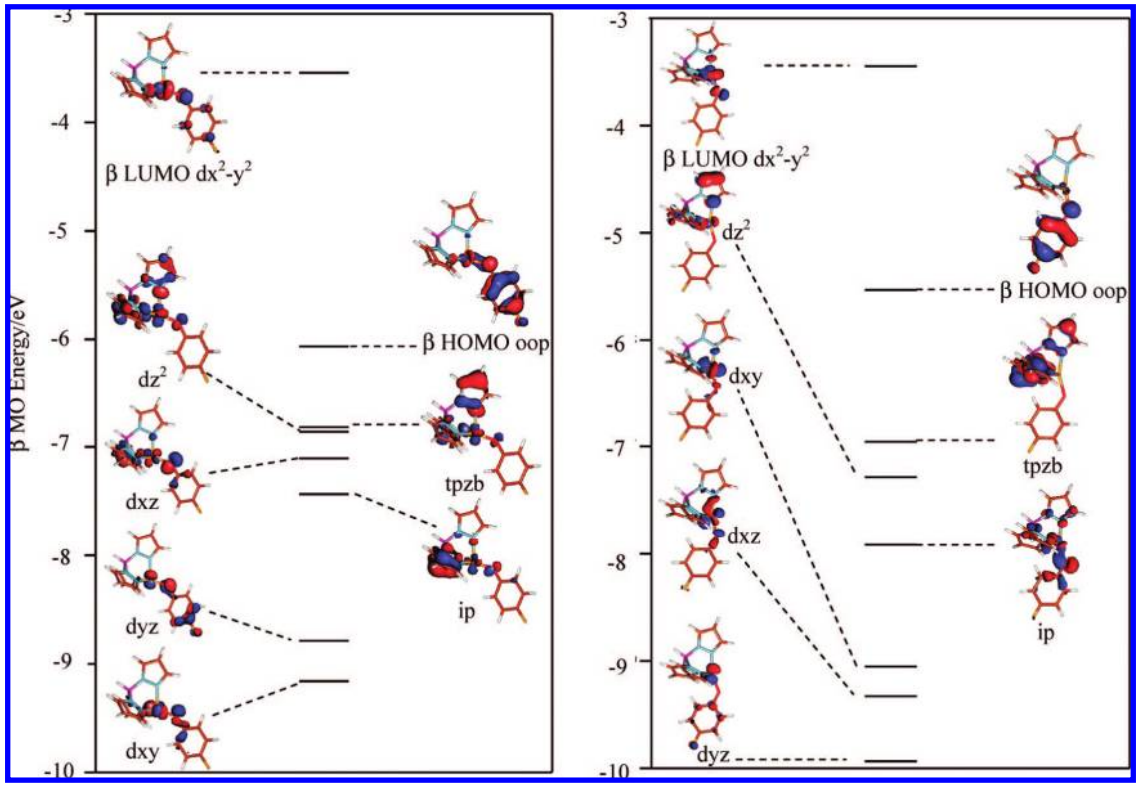

Figure 8. Simplified MO diagram of the β-MOs of L1 (left) and L3 (right), showing the LUMO, the HOMO (phenolate oop), the HOMO-1 (tpzb orbital), the five Cu d orbitals, and the phenolate ip orbital.

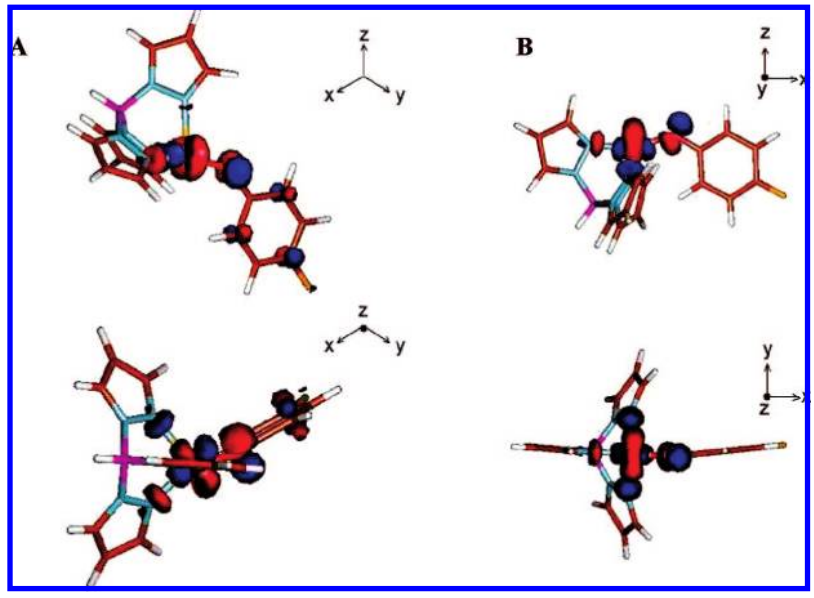

Figure 9. β LUMO of (A) L1 and (B) L3.

Table 7. Experimental vs Calculated *g* and *A* Values for L1 and L3[a]

compd	g_1	g_2	g_3	A_1	A_2	A_3
L1(exp)	2.320	2.135	2.010	5	67	120
L1(calc)	2.304	2.219	2.029	−9	−13	52
L3(exp)	2.317	2.125	2.005	0	20	143
L3(calc)	2.275	2.159	2.010	2	6	75

[a] The HFC values are provided in $\times 10^4$ cm^{-1}.

higher-energy ip phenolate → Cu CT transition (band 11), as the latter has little overlap with the β LUMO.

In the case of L3, the lower energy ip orbital has a bonding interaction with the LUMO (Figure 9B) which further stabilizes it. This results in a larger splitting of the ip and oop phenolate orbitals in L3 (Scheme 1, right) relative to the Zn^{II} reference complex. The oop phenolate orbital has little overlap with the β LUMO leading to a low-energy, very weak CT transition calculated to be at 5100 cm^{-1}. The good overlap between the ip phenolate orbital and the β LUMO results in an intense high-energy phenolate ip π → Cu CT transition (band 8, Figure 3).

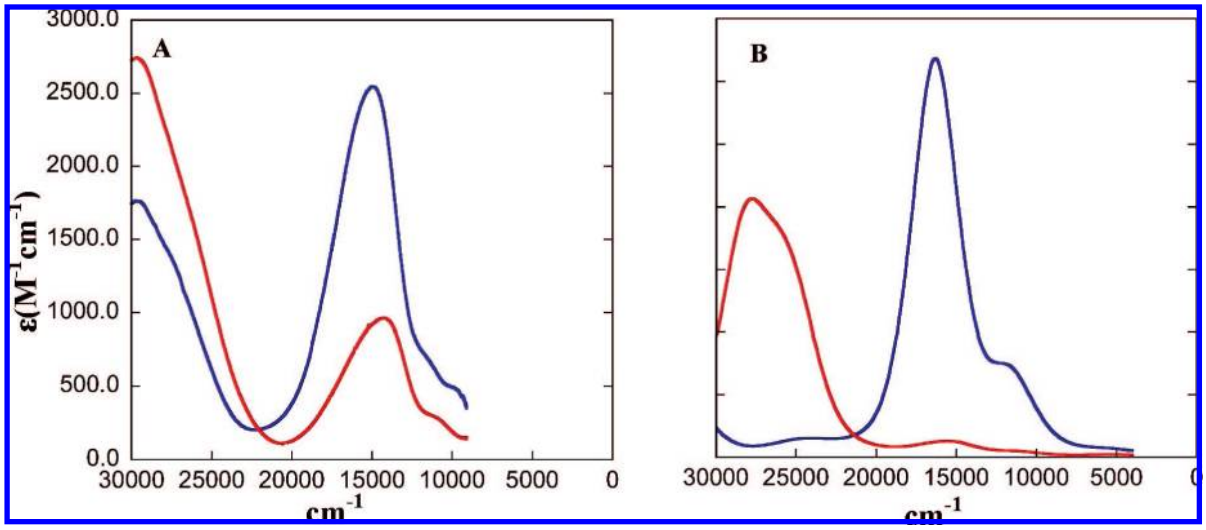

Figure 10. Overlay of L1 (blue) and L3 (red): (A) low-temperature experimental absorption spectra; (B) TD-DFT calculated absorption spectra.

Scheme 1. Splitting of the ip and oop Orbitals of the Free Phenolate (Center) and in Model Complexes $[M(NH_3)_3phenO]^+$ where M = Zn^{II} or Cu^{II}[a]

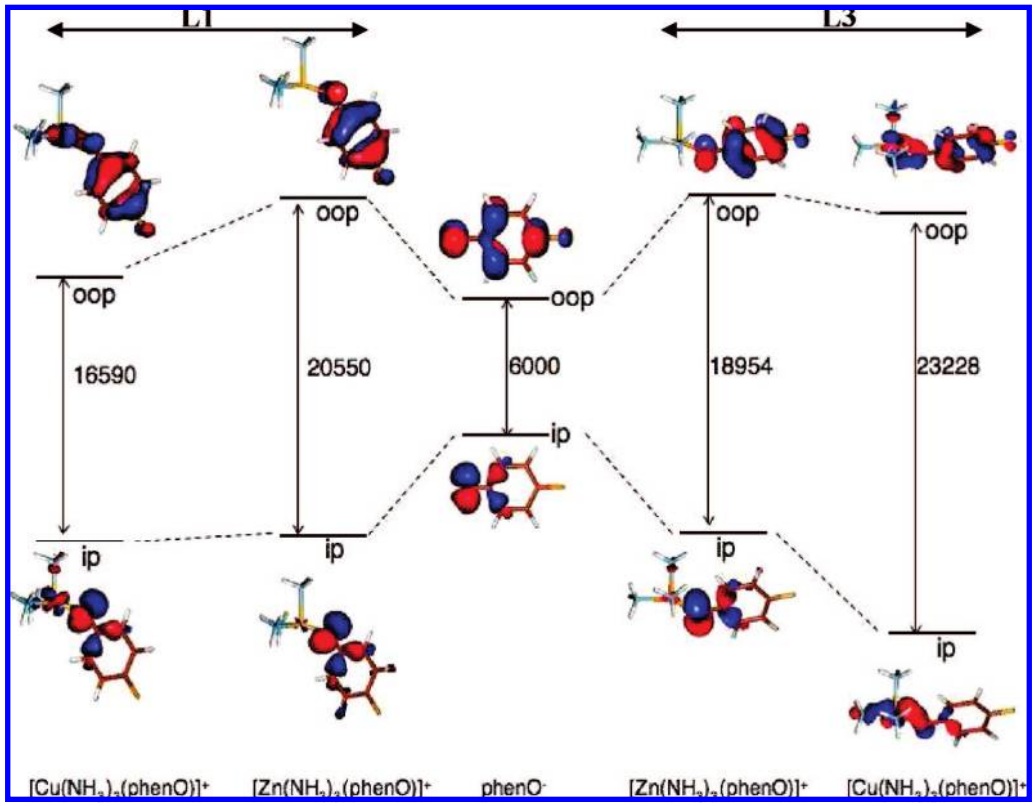

[a] Left side is for the L1 ring conformation, and the right side is for the L3 ring conformation. All energies are in cm^{-1}.

4.4. Reactivity. 4.4.1. Radical Character and its Contribution to Oxygen Reactivity. Calculations were performed on the L1 and L3 complexes by replacing the Cu^{II} by Zn^{II} and the phenolate by a phenoxyl radical to evaluate the amount of radical character in the phenolate ring for the Cu^{II} complexes compared to that of a phenoxyl radical bound to a metal center. Table 8 shows that the L1-Zn-phenoxyl and L3-Zn-phenoxyl complexes have 77% and 74% spin density on the phenoxyl ring, respectively. In contrast, the spin density on L1 is 14% and L3 is 9% (Table 6), with the spin density being delocalized in the oop phenolate orbital in L1 and in the ip phenolate orbital for L3. This shows that L1 is slightly more activated than L3, but more importantly, the amount of radical character in both L1 and L3 are small compared to their respective Zn-phenoxyl complexes.

Table 8. Spin Density Distribution of Zn Phenoxyl Complexes of L1 and L3

compd	Zn	phenO	tpzb
L1Zn	0.002	0.772	0.226
L3Zn	−0.007	0.745	0.262

To evaluate the possibility of O_2 attack on the ring of a phenoxyl radical in these copper complexes, the Gibbs free

Scheme 2. ΔG and Structures for the O_2 Attack on the ortho C in (from Left to Right) Phenoxyl, Zn^{II} Phenoxyl, L1 Cu^{II} Phenolate, and L3 Cu^{II} Phenolate[a]

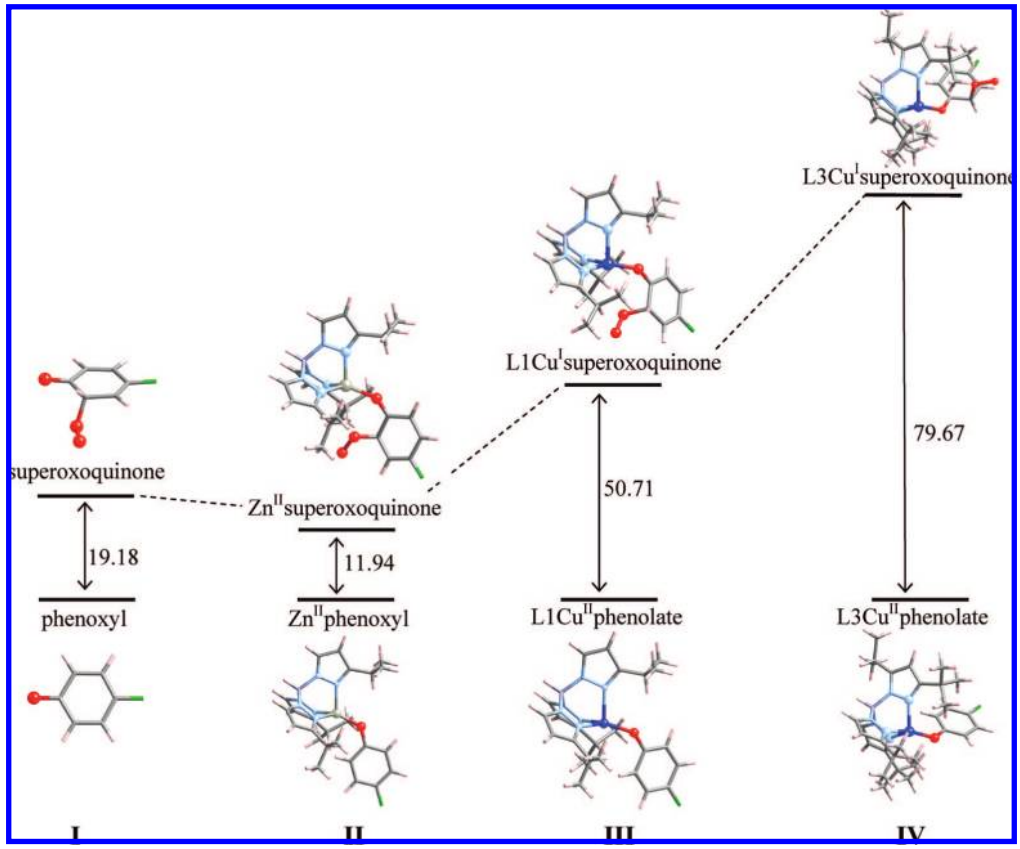

[a] All energies in kcal/mol.

energies of O_2 binding for different systems were compared. The ΔG for the reaction between a phenoxyl radical and O_2 is 19.2 kcal/mol (Scheme 2I). The ΔG for the O_2 attack on the L1 Zn-phenoxyl complex generating a Zn^{II} superoxoquinone decreases to 11.9 kcal/mol (Scheme 2II). This is due to the fact that the positively charged metal has an electrostatic interaction with the oxygen of the phenoxyl group. The amount of charge on the oxygen of the free phenoxyl radical is -0.25 compared to -0.86 for Zn^{II} phenoxyl. This electrostatic interaction polarizes the spin and activates the ring for O_2 attack.

The reaction of L1 Cu^{II} phenolate with O_2 oriented such that it cannot bind to the Cu^{II} results in the formation of a L1 Cu^{I} superoxoquinone complex with a ΔG of 50.7 kcal/mol (Scheme 2III). This reaction is calculated to involve a two-electron process. One electron is transferred from the oop phenolate orbital to the O_2, and the other electron transfers from this orbital to the singly occupied Cu^{II} d orbital. This LMCT process results in a Cu^{I} that parallels the LMCT band observed in the experimental absorption spectrum at 14730 cm^{-1} (42.1 kcal/mol). The high ΔG (50.7 kcal/mol) can be understood as related to the sum of the energy required to transfer an electron from phenolate $\rightarrow$ Cu^{II} (the LMCT transition, 42.1 kcal/mol) to create a phenoxyl radical and the energy of the O_2 reaction with this phenoxyl radical ($\sim$12 kcal/mol).

The full optimization of L3 Cu^{II} phenolate with O_2 results in a complex where the phenolate ring orientation is similar to that of the L1 complex. Therefore we introduced constraints in the optimization to restrict the ring in the L3 configuration. The calculated ΔG for the O_2 reaction in the L3 ring conformation is 80 kcal/mol (Scheme 2IV), which includes the LMCT transition (experimentally observed at higher energy, 27 850 cm^{-1}, because it requires CT from the ip orbital) combined with the reaction of O_2 with the resultant phenoxyl radical. All calculated energies are summarized in Scheme 2.

Finally, it should be noted that the experimental cyclic voltametry of L1 and L3 shows very low potential irreversible reduction peaks at -1215 mV and -1280 mV, respectively, against the ferrocene/ferrocenium couple. This indicates that the reduction of these complexes is extremely unfavorable, also inconsistent with the radical mechanism.

4.4.2. Cu Phenolate Reactivity. The ΔG for the reaction of dioxygen with phenol is 20 kcal/mol. The proton of the phenol transfers to the O_2 generating a hydroperoxoquinone (Scheme 3I). The ΔG for the O_2 reaction with a Zn phenolate complex (where Cu^{II} has been replaced by Zn^{II} in L1 configuration) leads to the formation of Zn^{II} peroxoquinone (22.3 kcal/mol, Scheme 3II), which is similar to the reference phenol complex. Thus, the tpzbZn^{II} group mimics the role of a proton. Note that for the structure in Scheme 3II, the phenolate species binds to Zn^{II} via the peroxo bridge instead of the quinone oxygen (Zn$-$O quinone bond length = 2.54 Å). When L1 Cu^{II} phenolate reacts with O_2 (allowing O_2 to bridge to Cu^{II}), the ΔG dramatically decreases to 11.3 kcal/mol (Scheme 3III), and the resulting complex is an L1 Cu^{II} peroxo bridged quinone forming a six-member ring, with the quinone O also bonded to Cu^{II} (Cu$-$O quinone bond length = 2.13 Å). To understand the significant difference in energies between the Zn^{II} and Cu^{II} phenolate reactions with O_2, geometry optimizations were performed on L1 Cu^{II} peroxoquinone keeping the $Cu^{II}-O$ (oxygen of the quinone) distance the same as in the Zn^{II} peroxoquinone

Scheme 3. ΔG and Structures for the O_2 Attack on the ortho C in (from Left to Right) Phenol, L1 Zn^{II} Phenolate, L1 Cu^{II} Phenolate, L1 Cu^{II} Phenolate (Cu−O Quinone Bond Length = 2.54 Å), and L3 Cu^{II} Phenolate[a]

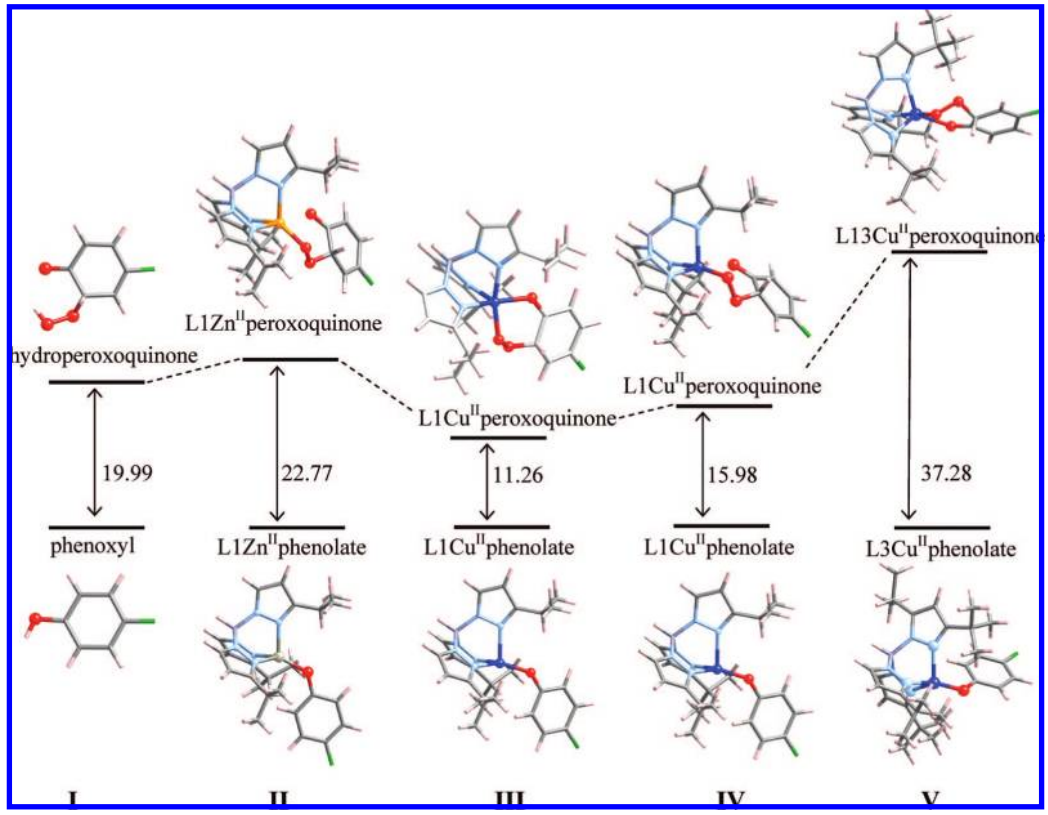

[a] All energies are in kcal/mol.

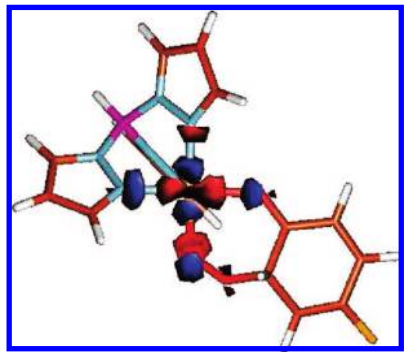

Figure 11. LUMO + 1 MO for L1 Cu^{II} peroxoquinone, showing the interaction between the $d_{x^2-y^2}$ orbital and the peroxobridge.

complex (2.54 Å, Scheme 3IV). The ΔG is 16 kcal/mol which is lower than that for the Zn^{II} phenolate/O_2 reaction. This indicates that bonding to the Cu^{II} is playing a role in the decreasing of the ΔG of O_2 attack. Inspection of the frontier MO for both the Zn^{II} peroxoquinone and L1Cu^{II} peroxoquinone reveals that while both have the same LUMO (antibonding quinone oop), L1 has the $d_{x^2-y^2}$ orbital as the LUMO + 1, while there is no such equivalent orbital in the Zn^{II} complex which is d^{10}. This LUMO + 1 in the Cu^{II} complex shows a strong bonding interaction between the $d_{x^2-y^2}$ orbital and the peroxo as well as some bonding with the O of the quinone (Figure 11). These additional σ bonding interactions between peroxoquinone and the Cu^{II} result in the lower ΔG for the O_2 reaction of the Cu^{II} relative to the Zn^{II} phenolate complex.

O_2 attack on L3 (phenolate ring constrained in L3 configuration) also results in the formation of an L3 Cu^{II} peroxoquinone (Scheme 3V), but with a ΔG of 37.3 kcal/mol. The higher ΔG is a consequence of the steric repulsion between the oxygen of the peroxobridge and two nitrogens of the tpzb system in the constrained structure. All energies are summarized in Scheme 3.

5. Discussion

The L1 and L3 complexes in Figure 1 provide two very different phenolate ring orientations due to the different steric requirements of the *iso*-propyl and *tert*-butyl substituents on the pyrazole ligand. These lead to very different frontier molecular orbitals. L1 has the oop phenolate *p*-orbital in a π bonding interaction with the Cu $d_{x^2-y^2}$ orbital, while L3 has the ip phenolate *p*-orbital in a pseudo-σ type interaction with the β LUMO (Figure 9). The different LUMOs of the two complexes lead to their very different spectroscopic properties. L1 has a smaller splitting between the ip and the oop phenolate CT transitions with a low-energy intense oop phenolate CT band. Alternatively, L3 has greater overlap of the ip phenolate π with the $d_{x^2-y^2}$ orbital and a larger energy splitting between the ip and the oop phenolate CT bands, having the intense ip phenolate CT transition at a higher energy (Scheme 1).

These differences in orientation lead to significant differences in bonding. The spin density on these complexes shows that L3 has less radical character (9%) compared with L1 (14%), though the amount of radical character in both is small compared to a reference Zn phenoxyl analogue (74−77%, Table 8). The O_2 reaction with L1 Cu^{II} phenolate forming a Cu^{I}superoxo-quinone species is ~29 kcal/mol more favored than the L3 analogue (Scheme 2) because of the presence of the lower energy phenolate LMCT transition in L1. Also the O_2 reaction

Scheme 4. Schematic Representation of Electron Transfer in the O_2 Reaction of L1 Cu^{II} Phenolate Forming the Cu^{II} Peroxoquinone

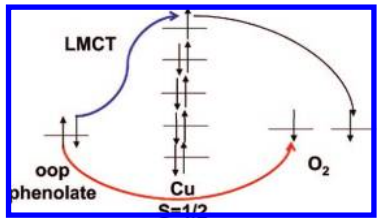

of Cu^{II} phenolate forming a Cu^{II} peroxoquinone species is ~26 kcal/mol more favorable for L1 than L3 (Scheme 3). Thus the L1 ring orientation is the preferred orientation for O_2 attack.

Importantly, the reaction of O_2 with L1 is not likely to proceed via a radical mechanism, since the amount of radical character in the ring is small. The energy for the radical reaction generating the superoxoquinone is high (51 kcal/mol), reflecting the energy of the associated LMCT transition. However, the energy of O_2 attack for L1 Cu^{II} phenolate to form a coordinated peroxoquinone is significantly lower (11.3 kcal/mol) than for the radical reaction and in fact for this reaction on the corresponding Zn^{II} phenolate complex or phenol (Scheme 3). The latter is due to the presence of an unoccupied $d_{x^2-y^2}$ orbital in Cu^{II} but not in d^{10} Zn^{II}. This orbital has good σ bonding interactions with the peroxy and O donor orbitals of the quinone, providing stabilization to form the bridging peroxoquinone.

The uncatalyzed O_2 reaction of organic substrates, like phenols, are kinetically slow because of their spin forbidden nature (O_2, $S = 1$; phenol, $S = 0$). It has been shown that an oxidized metal center can act as a buffer to catalyze the spin forbidden O_2 reaction with a coordinated substrate via a low-energy LMCT transition.[19] This model applied to L1 is depicted in Scheme 4, where the triplet O_2 is antiferromagnetically aligned with the Cu^{II} ($S = {}^1/_2$) due to orbital overlap along the reaction coordinate. The two-electron reduction of triplet O_2 from singlet phenolate could proceed by transferring one electron (spin up) from the phenolate directly onto the O_2 orbital which is σ bonded to the carbon and another electron (spin up) from Cu^{II} through a π interaction with the triplet O_2. The latter could be compensated by transferring an electron (spin down) from the phenolate ligand to Cu^{II} via the experimentally observed low-energy intense LMCT (14730 cm^{-1} band for L1) pathway. This results in a two-electron oxidation of a phenolate by triplet O_2 without affecting the oxidation state of the Cu^{II}. This mechanism does not require radical character in the ring and simply has the metal playing the role of a buffer in transferring an electron from the substrate to O_2 but of proper spin.

The generally proposed mechanism for the cofactor biogenesis of TPQ from tyrosine in amine oxidases invokes O_2 attack on a transient Cu^{I} tyrosyl radical species.[44,45] The present study on model systems indicates that the O_2 attack on the Cu^{II} phenolate yielding a radical Cu^{I}superoxyquinone is, in fact, energetically unfavorable (51 kcal/mol). Alternatively, the reaction free energy for O_2 attack on Cu^{II} phenolate generating a metallocycle Cu^{II} peroxoquinone species is only 11.3 kcal/mol which is comparable to the experimental barrier of 15 kcal/mol for TPQ formation (78 M^{-1} s^{-1} at high pH).[46] (This likely reflects the endergonic nature of the O_2 reaction combined with the lack of protons to drive the reaction. The latter would be present in the enzyme system.) In contrast to the radical reaction, this is spin forbidden. However as described above, a LMCT process can overcome this, and indeed an absorbance band is observed along the reaction coordinate of O_2 with Cu^{II} preprocessed enzyme.[14,15] These and other possible mechanisms for O_2 activation by a phenolate/tyrosine ring (e.g., H atom abstraction of the phenol proton by a $Cu^{II}OH^-$ site) need to be evaluated for the actual enzyme active site. We finally note that L1 has the more preferred ring orientation for O_2 attack and its ring orientation reflects the orientation of the tyrosine ring in the preprocessed active site of amine oxidase (Figure 1).

Acknowledgment. This research was supported by NIH Grant DK-31450 (E.I.S), by JSPS Grant (Scientific Research (B) 17350043) and by MEXT grant (Scientific Research on Priority Areas, 19020011) (K.F.). K.F. is grateful to Prof. K. Okamoto (University of Tsukuba) for his encouragement. S.G. is grateful for the William S. Johnson fellowship. J.C. is grateful to the Generalitat de Catalunya for the Beatriu de Pinos fellowship (2006 BP-A 10041).

Supporting Information Available: Coordinates for optimized geometries, ΔG for O_2 binding to phenol, phenoxyl, and phenolate in both spin states, complete MO diagrams, complete reference 27, and cif files of L1 and L3. This material is available free of charge via the Internet at http://pubs.acs.org.

JA8044986

(44) Ruggiero, C. E.; Smith, J. A.; Tanizawa, K.; Dooley, D. M. *Biochem.* **1997**, *36*, 1953.
(45) DuBois, J. L.; Klinman, J. P. *Arch. Biochem. Biophys.* **2005**, *433*, 255.
(46) Note that there is no observed reactivity of L1 and L3 with O_2 in dry dichloromethane solvent.